NANO LETTERS

pubs.acs.org/NanoLett

Letter

Electron Beam Infrared Nano-Ellipsometry of Individual Indium Tin Oxide Nanocrystals

Agust Olafsson,[⊥] Jacob A. Busche,[⊥] Jose J. Araujo, Arpan Maiti, Juan Carlos Idrobo, Daniel R. Gamelin,* David J. Masiello,* and Jon P. Camden*

Cite This: *Nano Lett.* 2020, 20, 7987−7994

Read Online

ACCESS | Metrics & More | Article Recommendations | Supporting Information

ABSTRACT: Leveraging recent advances in electron energy monochromation and aberration correction, we record the spatially resolved infrared plasmon spectrum of individual tin-doped indium oxide nanocrystals using electron energy-loss spectroscopy (EELS). Both surface and bulk plasmon responses are measured as a function of tin doping concentration from 1−10 atomic percent. These results are compared to theoretical models, which elucidate the spectral detuning of the same surface plasmon resonance feature when measured from aloof and penetrating probe geometries. We additionally demonstrate a unique approach to retrieving the fundamental dielectric parameters of individual semiconductor nanocrystals via EELS. This method, devoid from ensemble averaging, illustrates the potential for electron-beam ellipsometry measurements on materials that cannot be prepared in bulk form or as thin films.

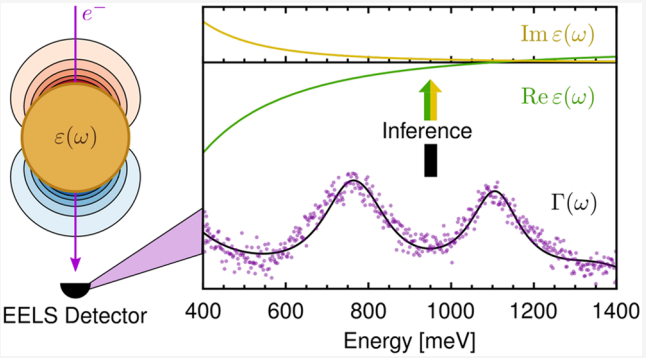

KEYWORDS: *infrared plasmonics, electron energy-loss spectroscopy, doped semiconductor nanocrystals*

Carrier doped semiconductor nanocrystals (NCs) are an emerging class of materials with tunable near-to-mid infrared (IR) optical responses that vary with dopant concentration.[1−7] Similar to noble metals, doped semiconductors have sufficient free carrier densities (10^{18}−10^{20} cm^{-3}) to produce localized surface plasmon (LSP) and bulk plasmon resonances.[8−14] In addition to greatly expanded IR tunability, doped NCs are also attractive because they offer IR plasmonic responses at truly nanoscale dimensions, something that typically cannot be achieved in noble metal nanostructures.[15−19] Beyond these qualities, altering geometric properties such as size, shape, and aggregation provides another route to exert control over their spectrum.[20−22] Due to this versatility, NC materials are being harnessed for applications such as surface-enhanced infrared absorption,[23,24] molecular sensing,[25−27] medical therapeutics and imaging,[28,29] photovoltaics,[30,31] and photocatalysis[32−34] among many others.

Heterogeneity between NCs leads to spectral broadening of plasmon resonances in ensemble measurements,[35] making the study of individual NCs essential for the development and application of IR plasmons.[18,36] Studying the IR responses of individual NCs, however, is limited by instrumentation challenges. At these wavelengths, the diffraction limit is much larger than the NCs themselves (≳1 μm versus <50 nm, respectively), making dark field scattering[37,38] and interferometric methods[39,40] ineffective. Alternatively, near-field scanning optical microscopy (NSOM)[41,42] is hampered by the lack of bright IR light sources and high quantum efficiency detectors. Nevertheless, when coupled to a synchrotron radiation source, NSOM variants like synchrotron infrared nanospectroscopy (SINS) have been used to measure the IR plasmons in individual NCs[43−45] and have found their resonance energies and line widths to differ from ensemble values. The limited spectral range (∼100−600 meV) of SINS,[43] however, has precluded the characterization of NC responses over a wide range of plasmon energies.

Recent advances in aberration correction and monochromation of scanning transmission electron microscopes (STEMs) have driven the energy resolution of electron energy-loss spectroscopy (EELS) as low as ∼5 meV (40 cm^{-1}), enabling the study of IR materials responses for the first time.[46−48] Despite these developments, there have been no studies of the dependence of NC plasmons on dopant concentration at the single-particle level. Additionally, no methods exist to retrieve the underlying dielectric parameters of individual NCs that give rise to IR plasmons. Herein, we use high-resolution monochromated STEM-EELS to characterize

Received: July 8, 2020
Revised: August 31, 2020
Published: September 1, 2020

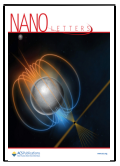

the broad-band spectral evolution of the surface and bulk plasmons of individual tin-doped indium oxide (ITO) NCs by controlling the relative number of free carriers per NC through Sn^{4+} dopant concentration. Our results are combined with theoretical modeling to extract the underlying material parameters that give rise to this spectral tunability, thereby informing the rational design of future NC-based plasmonic materials with desired IR responses.

ITOs are a well-studied group of optoelectronic conductive metal oxides that have been characterized as thin films and substrates over the past several decades due to their dopant-induced metallic behavior,[49,50] and extensive dielectric data are available.[51−53] The plasmonic properties of various colloidal ITO NCs have also been reported, but these have primarily focused on ensemble properties[54−60] leaving few single particle studies to date.[61,62] Utilizing an established synthetic strategy,[58] we chemically grow ∼20 nm diameter colloidal NCs of ITO with Sn^{4+} dopant concentrations of 1, 2, 5, 7.5, and 10 atomic percent, as well as an undoped In_2O_3 NC sample. Targeting this size avoids associated complications encountered at larger and smaller sizes. For example, as NCs increase in size their LSP resonances red-shift[35,63] and can become buried in the zero-loss (elastic scattering) peak of the EEL spectrum, while quantum confinement and spill-out effects induce complex changes to the LSP energies for smaller NCs.[64−67] These NCs have free carrier densities on the order of 10^{20}−10^{21} cm^{-3}, depending on the dopant concentration.[57−59]

Figure 1a shows a representative TEM image of 10% ITO NCs cast from bulk, displaying NC geometries ranging from cuboid to spherical. To minimize interparticle and particle−environment interactions in the STEM-EELS measurements, dilute NC solutions are cast onto 5 nm thick amorphous SiN grids. The NCs are then stripped of their native oleate ligands by submerging the sample in an acetonitrile solution of $(Et_3O)BF_4$.[68] Due to the sensitive nature of the LSP to particle geometry, the high-angle annular darkfield (HAADF) images (Figure 1b inset) are inspected for faceting and cornering and to select only the most spherical NCs for measurement. While cubic nanoparticles have spectrally distinct multipolar LSPs,[69−71] the splitting is less pronounced in spherical-cuboid particles and may only effectively broaden the dipolar plasmon resonance feature depending on the degree of edge and corner formation (Supporting Information (SI)).

All EEL spectra are collected on an aberration corrected and monochromated STEM operating at 60 kV with 20 mrad and 20 mrad convergence and collection angles, and an approximately 18 meV zero-loss peak at full width at half-maximum (fwhm). Two impact parameters are recorded (Figure 1b) for each NC. First, an aloof position (red) is recorded 5 nm away from the NC surface, with the resulting point spectrum showing an LSP resonance feature. This feature is symmetric and does not appear to overlap other spectrally distinct resonances, suggesting that deviations from spherical geometry are minimal. Second, a penetrating trajectory (blue) passing through the center of the particle is recorded with the resulting point spectrum exposing two resonance features, one due to the LSP responses and the other to the bulk plasmon as modified by the finite NC boundaries. The spectrum images in Figure 1c confirm this identification, and the uniform EEL probability distribution of the surface plasmon mode profile supplies additional evidence for the NC's effectively spherical symmetry.

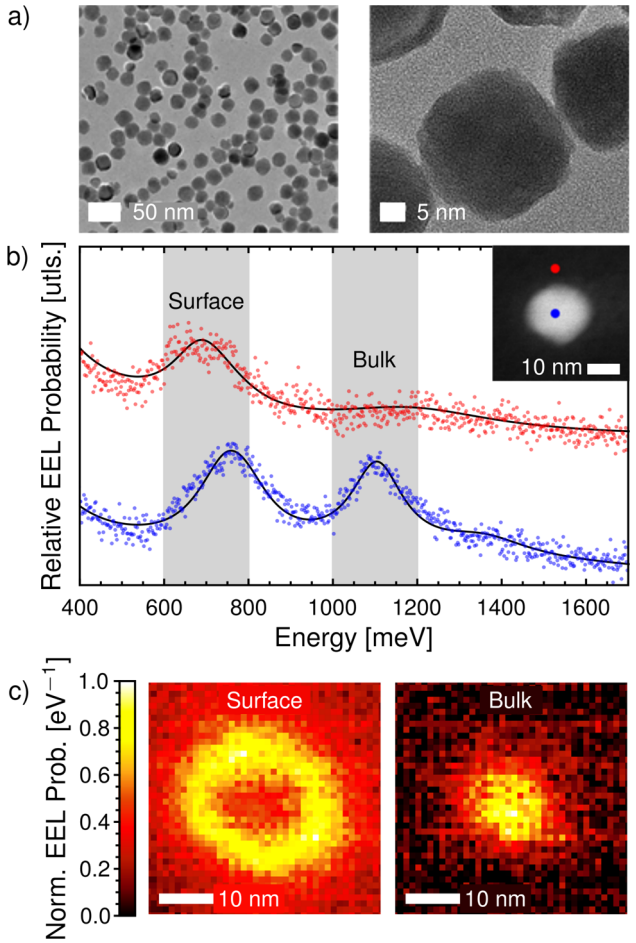

Figure 1. Representative ITO NC images and EEL spectra. (a) TEM images of a 10% Sn^{4+} doped ITO NC sample displayed at two different magnifications, showing heterogeneity in NC shape and size. (b) Characteristic aloof (red, $b - a = 5$ nm) and penetrating (blue, $b = 0$ nm) EEL spectra of an individual 7.5% Sn^{4+} doped ITO NC, along with best numerical fits. The inset shows an HAADF image of the NC along with the two probe positions. Interestingly, the surface plasmon resonance energies are observed to differ between aloof and penetrating spectra. (c) Spectrum images of the same NC acquired at the surface and bulk plasmon peak energies.

Figure 2a shows substrate subtracted aloof (upper) and penetrating (lower) EEL spectra recorded for individual ITO NCs ranging from 1% to 10% Sn^{4+}. In general, the peak energies of the LSPs and bulk plasmons exhibit a gradual blue shift as the Sn^{4+} concentration increases, which is consistent with ensemble measurements of ITO colloids.[55,57] This result also agrees with studies that measure the electrical properties of ITO thin films, which show that increased doping increases the electron density and lowers the resistivity.[52,72] This behavior is directly correlated to the changing crystal structure of the In_2O_3 by the substitution of an In^{3+} ion with a Sn^{4+} ion in the In_2O_3 lattice, providing an available free carrier.[52] As shown in Figure 2b, the plasmon energy shows a nonlinear dependence on the dopant concentration, leveling off around 10%. Once again, this result is consistent with previous analysis, which suggests that, at higher concentrations of Sn^{4+}, crystal defects and trap state formation begin to affect the particle's electrical properties.[52,73] Additionally, changes to the atomic structure of the NCs, especially at the surface, may be

https://dx.doi.org/10.1021/acs.nanolett.0c02772
Nano Lett. 2020, 20, 7987−7994

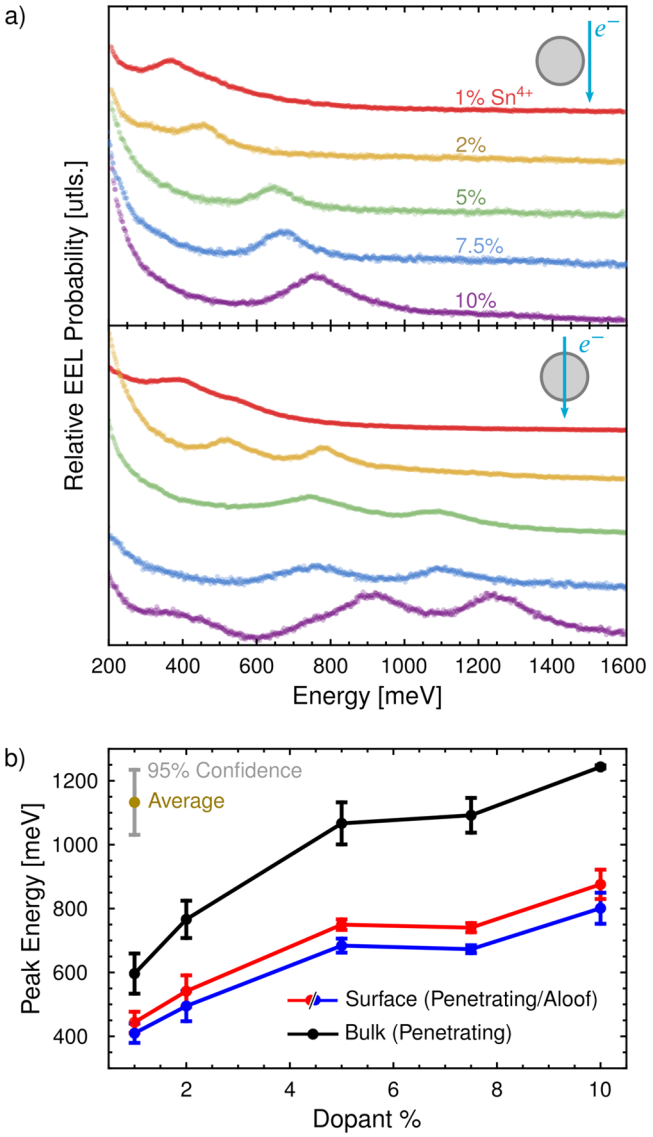

Figure 2. EEL spectra of individual ITO NCs as a function of Sn^{4+} dopant concentration. (a) Both surface and bulk plasmon resonance energies increase as the Sn^{4+} dopant concentration increases from 1−10 atomic percent for both aloof (upper) and penetrating (lower) beam trajectories. (b) Average surface and bulk plasmon resonance energies and 95% confidence intervals for all measured point spectra at all dopant concentrations. Note that the surface plasmon resonance profile differs between aloof and penetrating spectra of the same particle due to the differing multipolar contributions driven by the electron probe at each position.

responsible for the variation in individual particle resonance energies and line widths measured (SI).[59,74]

Examination of the data further reveals a surprising difference between LSP energies depending upon the location of the electron probe. Although the spectrum images in Figure 1c identify the lower energy resonance peak as the LSP, they do little to explain the ∼100 meV energy shift observed in the point spectra recorded for aloof and penetrating beam trajectories of the same LSP resonance feature. The origin of this shift can be understood theoretically by considering the inelastic electron scattering from a spherical particle containing the bulk free-electron gas dielectric function $\varepsilon(\omega) = \varepsilon_\infty - \omega_p^2/(\omega^2 + i\omega\gamma)$. Here, ω_p is the semiconductor's plasma frequency, γ is its electron−ion scattering rate, and ε_∞ is its high frequency dielectric constant. Retardation effects and the response of the substrate (∼5 nm thick SiN) to the fields of the electron are neglected as the small NC sizes (<25 nm) and low carrier densities studied justify working in the quasistatic approximation with negligible substrate-induced plasmon mode mixing.[71]

Under these assumptions, the Laplace equation can be solved exactly and used to determine the EEL probability function for both aloof and penetrating beam trajectories (SI).[75,76] Fundamental to the solution is Green's function G, which encodes the complete set of bulk and geometry-induced surface responses of the target system. When probed by a fast electron with charge density $\rho(\mathbf{x}, t) = -e\delta(\mathbf{R} - b\hat{\mathbf{R}})\delta(z + vt)$, the potential at the arbitrary point $(\mathbf{x}, t)$ is the superposition of independent Coulombic and induced plasmonic components defined by

$$\Phi(\mathbf{x}, t) = \int_{-\infty}^{t} dt' \int d^3x' G(\mathbf{x}, t; \mathbf{x}', t')\rho(\mathbf{x}', t') \tag{1}$$

where $G = G_0 + G_{ind}$ similarly factors into the sum of a direct Coulombic response $G_0 = 1/|\mathbf{x} - \mathbf{x}'|$ to the STEM electron and the induced responses

$$\begin{aligned} G_{ind}^{r'' <a}(\mathbf{x}, \mathbf{x}'; \omega) = &\left\{ \frac{g_\infty(\omega)}{|\mathbf{x} - \mathbf{x}'|} + \frac{1}{a}\sum_{lm} [g_l^<(\omega) - g_B(\omega)] \right. \\ &\left. f_{lm}^<(\mathbf{x}) f_{lm}^{<*}(\mathbf{x}') \right\} \Theta(a - r) \\ &+ \frac{1}{a}\sum_{lm} g_l^{><}(\omega) f_{lm}^>(\mathbf{x}) f_{lm}^{<*}(\mathbf{x}') \Theta(r - a), \\ G_{ind}^{r' >a}(\mathbf{x}, \mathbf{x}'; \omega) = &-\frac{1}{a}\sum_{lm} g_l^>(\omega) f_{lm}^>(\mathbf{x}) f_{lm}^{>*}(\mathbf{x}') \Theta(r - a) \\ &+ \frac{1}{a}\sum_{lm} g_l^{><}(\omega) f_{lm}^<(\mathbf{x}) f_{lm}^{>*}(\mathbf{x}') \Theta(a - r) \end{aligned} \tag{2}$$

set up by the target, taken to be a sphere of radius a. The latter are expressed in their spectral representation in terms of the surface and bulk response functions $g_l^>(\omega) = l[\varepsilon(\omega) - 1]/(l\varepsilon(\omega) + l + 1)$, $g_l^<(\omega) = (2l + 1)/(l\varepsilon(\omega) + l + 1)$, $g_l^{><}(\omega) = g_l^<(\omega) - 1$, and $g_B(\omega) = 1/\varepsilon(\omega)$, $g_\infty(\omega) = g_B(\omega) - 1$, each dependent upon $\varepsilon(\omega)$. Together, they set the time dynamics of the ITO plasmon responses including their natural frequencies, line widths, and effective masses. For example, it is from the poles of the surface response functions $g_l^>$, $g_l^<$, and $g_l^{><}$, which depend on the multipole order l, that the natural frequencies $\omega_l = \omega_p\sqrt{l/(l\varepsilon_\infty + l + 1)}$ of the LSPs are defined, while the bulk plasmon frequency[77,78] $\omega_B = \omega_p/\sqrt{\varepsilon_\infty}$ is defined by the pole of the bulk response functions g_B and g_∞. The spatial variation of G_{ind} is determined by the (l, m)-dependent LSP mode functions

$$f_{lm}^{<,>}(\mathbf{x}) = \sqrt{4\pi/(2l + 1)}\, Y_{lm}(\hat{\mathbf{x}})\{(r/a)^l, (a/r)^{l+1}\}$$

with $\mathbf{x} = (\mathbf{R}, z)$ and $r = |\mathbf{x}| = \sqrt{|\mathbf{R}|^2 + z^2}$ (see SI).

As the localized electron probe travels near or through the NC, it interacts with its plasmon modes, losing a small fraction

https://dx.doi.org/10.1021/acs.nanolett.0c02772
Nano Lett. 2020, 20, 7987−7994

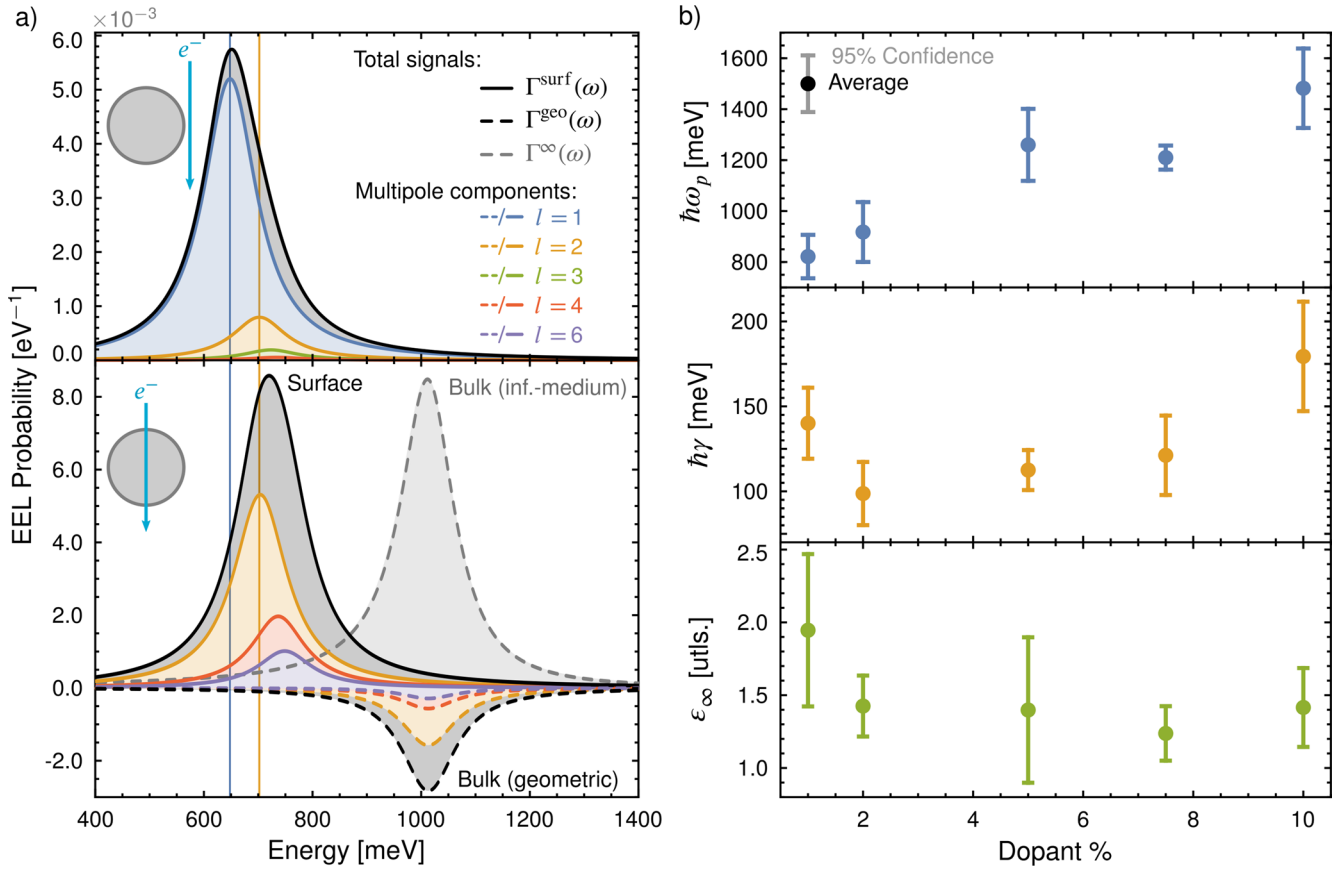

Figure 3. Theoretical analysis of the inelastic electron scattering function $\Gamma(\omega)$ for both aloof and penetrating trajectories. (a) The relative contributions of $\Gamma^{\mathrm{surf}}(\omega)$, $\Gamma^{\mathrm{geo}}(\omega)$, and $\Gamma^{\infty}(\omega)$, along with their multipolar decompositions, to $\Gamma(\omega)$ at aloof (upper, $b - a = 5$ nm) and penetrating (lower, $b = 0$ nm) beam positions show the origin of the observed shift between aloof and penetrating spectra of the same LSP resonance feature. (b) Extracted Drude dielectric parameters from numerical fits of $\Gamma(\omega)$ to the full set of individual NC data. The variance-weighted average values of the plasma frequency ω_p (blue), electron−ion scattering rate γ (yellow), and high-frequency dielectric constant ε_∞ (green) at each dopant concentration are shown with points, with the parameter variances estimated from each fit. 95% confidence intervals are shown with error bars.

$\hbar\omega$ of its initial kinetic energy $mv^2/2$ with probability $\Gamma(\omega) = \Gamma^{\mathrm{surf}}(\omega) + \Gamma^{\mathrm{geo}}(\omega) + \Gamma^{\infty}(\omega)$ per unit energy loss. Each contribution arises from the work done by the electron's induced potential upon itself via

$$\Gamma(\omega) = -\frac{1}{\pi\hbar^2}\int \mathrm{d}^3x\, \mathrm{d}^3x'\, \mathrm{Im}\{\rho^*(\mathbf{x}, \omega)\, G_{\mathrm{ind}}(\mathbf{x}, \mathbf{x}'; \omega)\, \rho(\mathbf{x}', \omega)\} \tag{3}$$

where both $\mathbf{x}$ and $\mathbf{x}'$ extend over all space and include configurations where $r, r' > a$, $r, r' < a$, and $r < a$, $r' > a$ and vice versa. The first term

$$\Gamma^{\mathrm{surf}}(\omega) = -\frac{1}{a\pi\hbar^2}\sum_{lm} |A_{lm}^{>}(\omega)|^2\, \mathrm{Im}\, g_l^{>}(\omega) + |A_{lm}^{<}(\omega)|^2 \mathrm{Im}\, g_l^{<}(\omega) + 2\mathrm{Re}\{A_{lm}^{>}(\omega) A_{lm}^{<}(\omega)\} \mathrm{Im}\, g_l^{><}(\omega) \tag{4}$$

describes the energy losses due to excitation of LSPs. The functions $A_{lm}^{<,>}(\omega) = \int_{V_{<,>}} \rho^*(\mathbf{x}, \omega) f_{lm}^{<,>}(\mathbf{x}) d^3x$ are projection integrals of the electron's charge density against the LSP mode functions along the electron's trajectory through the volumes within ($V_<$) and outside ($V_>$) of the NC. These trajectory integrals dictate the change in magnitude of the response of each LSP mode as the impact parameter b is varied relative to the sphere radius a.

The latter two terms of $\Gamma(\omega)$ are the geometry-induced and infinite-medium contributions to the bulk plasmon response, given by

$$\Gamma^{\mathrm{geo}}(\omega) = \frac{1}{a\pi\hbar^2}\sum_{lm} |A_{lm}^{<}(\omega)|^2\, \mathrm{Im}\, g_B(\omega)$$

$$\Gamma^{\infty}(\omega) = -\frac{2e^2 \mathrm{Re}\{\sqrt{a^2 - b^2}\}}{\pi\hbar^2 v^2} \ln\left(1 + \frac{k_c^2 v^2}{\omega^2}\right) \mathrm{Im}\, g_\infty(\omega). \tag{5}$$

These contributions have opposite signs: the geometric bulk plasmon terms (Γ^{geo}) serve to reduce the overall bulk plasmon EEL probability and are responsible for the well-known *begrenzungseffekt* (see Figure 3a),[75,79,78] while the infinite medium term (Γ^{∞}) is directly proportional to the path length of the electron's trajectory within the ITO NC, $2\sqrt{a^2 - b^2}$, and is dependent on the quantity k_c. This is a cutoff wavenumber that imposes a smoothing of the lateral components of the bulk plasmon's polarization response as the electron passes through the sphere and is defined by the half-aperture collection angle of the STEM spectrometer.[79] Without this cutoff, $\Gamma^{\infty} \to \infty$ as $k_c \to \infty$ (SI).

The contributions of each of these terms to the total EEL signal are highlighted in Figure 3a. First, the bulk plasmon contributions are zero when the beam passes outside the

https://dx.doi.org/10.1021/acs.nanolett.0c02772
Nano Lett. 2020, 20, 7987−7994

particle, as $A_{lm}^{<}(\omega) = 0 = \mathrm{Re}\{\sqrt{a^2 - b^2}\}$ for $b > a$. In this case, the total signal is almost entirely determined by the dipolar ($l = 1$) LSP mode. As the beam approaches the surface, contributions from the higher-order l modes increase until the probe penetrates the sphere. For penetrating trajectories, the signal contains significant contributions from both the surface and bulk plasmon responses. The bottom panel of Figure 3a demonstrates the relative magnitudes of each multipole contribution to both Γ^{surf} and Γ^{geo}, as well as the magnitude of Γ^{∞}. It is important to note that the relative contribution from each multipole l changes as the probe is brought inside the particle. For $b/a = 0$, the odd-parity modes contribute negligibly while the even-parity modes $2 \leq l \lesssim 10$ dominate the signal, shifting the apparent LSP peak position to a higher energy relative to the LSP resonance in the aloof spectrum. This effect explains the detuning between the aloof and penetrating LSP peak positions of the surface modes observed in Figure 2b.

Because they contain responses at both surface and bulk plasmon energies, the penetrating trajectory EEL data allow for the extraction of unique values for the dielectric parameters ω_p and ε_∞ from the surface and bulk plasmon peak positions via nonlinear least-squares fitting to $\Gamma(\omega)$ in eqs 1 and 2. The peak line widths are determined completely by γ in the quasistatic limit so that the bulk electron−ion scattering rate can also be uniquely determined from the same fitting routine. Extraction of these peak parameters, however, is obstructed by numerous processes in the low-loss region (<5 eV).[80,81] Such processes are considered background when studying LSPs and can be removed through a variety of standard techniques, the suitability of which is specific to the system being probed.[48,82,83] Prior to fitting, we perform a background subtraction using the signal obtained from a nonplasmonic In_2O_3 NC positioned on an identical 5 nm thick SiN substrate.[84−86] Heuristic fitting of the penetrating EEL spectrum of a similarly sized In_2O_3 NC (SI) acts as reference which we use to fit the inelastic scattering due to the collective excitation of free carriers in ITO at each Sn^{4+} doping concentration (SI).

Once the plasmon signals are properly isolated from the background, two theoretical scale parameters, N and k_c, are tuned to normalize the total signal and align the relative heights of the theoretical surface and bulk peaks to their experimental values (SI). Importantly, The extraction of ω_p, γ, and ε_∞ from the data relies only on knowledge of the peak positions and line widths so that no parameter is affected by the values of N and k_c chosen. Because acquiring absolute EEL probabilities from experiments is difficult, even in modern STEMs, the independence of the Drude parameters from the scale parameters makes determining the dielectric properties of individual NCs dramatically more feasible. Extension of this approach to materials that are better characterized by a Drude−Lorentz dielectric model is straightforward but requires additional aloof and penetrating point spectrum measurements to uniquely resolve the additional fit parameters.

In this manner, the Drude parameter values are inferred from 28 separate penetrating trajectory EEL spectra of ITO NCs ranging from 16 to 24 nm in diameter and with Sn^{4+} dopant concentrations in the range 1−10 atomic percent. An additional 22 separate aloof-beam measurements (which do not contain bulk plasmon signals) are used to provide further estimates of γ, for which the existence of two observable peaks is not necessary. Results of the parameter extraction are shown in Figure 3b. They show that the plasma frequency increases with the addition of free carriers in a nonlinear fashion that approaches a maximum around 10% Sn^{4+} composition. The lowest inferred value of $\hbar\omega_p$ is 705 meV at 1% Sn^{4+}, while the highest is 1575 meV at 10% Sn^{4+}, corresponding to a range of carrier densities of 1.12×10^{20} to 5.58×10^{20} cm^{-3}, consistent with refs 73 and 87−89 when assuming a free carrier effective mass of $m^* = 0.31m$.[88,90−92]

Fit values of $\hbar\gamma$, the fwhm of the bulk plasmon peak as well as each multipole component of the LSP peak, are slightly higher at low and high Sn^{4+} concentrations than at intermediate levels of doping, with a dip at 2% Sn^{4+} where the fit average is 99 meV, which corresponds to 1.30−2.10 times the Drude damping rate of gold extracted with modern methods.[93,94] These results are also in good agreement with established thin film measurements of ITO.[87−89] Beyond these comparisons, this approach further opens up the potential of STEM-EELS to investigate the dependence of other factors such as grain boundaries,[95−97] surface depletion layers,[59,60,74] and environmental effects upon γ at the single particle level.[3,21,23,56]

Finally, the extracted values of ε_∞ are tightly grouped around 1.369 ± 0.025 for all dopant concentrations except for 1%, which shows an abrupt increase to 1.950. These results disagree with earlier measurements on thin films[87−89] that suggest ε_∞ to be near 4. We do not speculate on the physical origin of these ε_∞ differences between thin films, NC ensembles, and individual NCs, but point out that hybridization between the LSPs of different NCs or with environmental resonances is suppressed at values of ε_∞ greater than ~1[98] (SI). Despite this observation, the thin (~5 nm) SiN substrates used[71] and minimization of NC corner features diminish the NC−environment interactions in the present study. However, extraction of ε_∞ values near unity suggests that ITO NC plasmons should be capable of hybridizing into collective IR resonances that are additionally tunable by LSP coupling strength and detuning.

In summary, we use high-resolution monochromated STEM-EELS to characterize the evolution of the IR plasmon spectrum in individual ITO NCs with changing dopant concentration for the first time. We show that increasing the free carrier density via increased Sn^{4+} concentration is an effective method for tuning plasmon responses over a wide range of IR energies and that individual NC heterogeneity can easily account for broad LSP responses measured by ensemble averages. Furthermore, we use a numerical fitting procedure to extract the frequency-dependent ITO Drude dielectric function at each Sn^{4+} concentration from 1 to 10 atomic percent. By modeling the surface and bulk plasmon responses, this approach demonstrates the ability of STEM-EELS to determine dielectric material parameters in a single measurement and with less difficulty than standard thin film ellipsometry methods, paving the way for the facile retrieval of dielectric information from other doped semiconductor NCs at the single particle level. This work further demonstrates a route to extract key materials properties normally obtained from ellipsometry measurements but on materials that cannot be prepared in bulk form or as thin films.

https://dx.doi.org/10.1021/acs.nanolett.0c02772
Nano Lett. 2020, 20, 7987−7994

■ ASSOCIATED CONTENT

Supporting Information

The Supporting Information is available free of charge at https://pubs.acs.org/doi/10.1021/acs.nanolett.0c02772.

Information on additional penetrating and aloof EEL point spectra illustrating the variation in peak energy and line width for individual particles of the same dopant concentration, the mathematical derivation of the penetrating and aloof EEL functions, and the theory of plasmon mode mixing (PDF)

■ AUTHOR INFORMATION

Corresponding Authors

Daniel R. Gamelin − *Department of Chemistry, University of Washington, Seattle, Washington 98195, United States;* orcid.org/0000-0003-2888-9916; Email: gamelin@uw.edu

David J. Masiello − *Department of Chemistry, University of Washington, Seattle, Washington 98195, United States;* orcid.org/0000-0002-1187-0920; Email: masiello@uw.edu

Jon P. Camden − *Department of Chemistry and Biochemistry, University of Notre Dame, Notre Dame, Indiana 46556, United States;* orcid.org/0000-0002-6179-2692; Email: jon.camden@nd.edu

Authors

Agust Olafsson − *Department of Chemistry and Biochemistry, University of Notre Dame, Notre Dame, Indiana 46556, United States*

Jacob A. Busche − *Department of Chemistry, University of Washington, Seattle, Washington 98195, United States;* orcid.org/0000-0003-4797-9415

Jose J. Araujo − *Department of Chemistry, University of Washington, Seattle, Washington 98195, United States;* orcid.org/0000-0003-0955-2584

Arpan Maiti − *Department of Chemistry and Biochemistry, University of Notre Dame, Notre Dame, Indiana 46556, United States*

Juan Carlos Idrobo − *Center for Nanophase Materials Sciences, Oak Ridge National Laboratory, Oak Ridge, Tennessee 37831, United States*

Complete contact information is available at: https://pubs.acs.org/10.1021/acs.nanolett.0c02772

Author Contributions

⊥A.O. and J.A.B. contributed equally.

Notes

The authors declare no competing financial interest.

■ ACKNOWLEDGMENTS

Work at the University of Notre Dame (A.O., J.P.C.) was supported by the U.S. Department of Energy (DOE), Office of Science, Office of Basic Energy Sciences (BES), Materials Sciences and Engineering Division under Award DE-SC0018169, as well as by the HERE program at Oak Ridge National Laboratory (A.O.). Work at the University of Washington was supported by the U.S. Department of Energy (DOE), Office of Science, Office of Basic Energy Sciences (BES), Materials Sciences and Engineering Division under Award DE-SC0018040 (J.A.B., D.J.M.), by the U.S. National Science Foundation under Award CHE-1904436 (J.J.A., D.R.G.), and by the SCGSR Fellowship Program operated by the Oak Ridge Institute for Science and Education (J.A.B.). The STEM experiments were conducted at the Center for Nanophase Materials Sciences, which is a DOE Office of Science User Facility (J.C.I.). This research was conducted, in part, using instrumentation within ORNL's Materials Characterization Core provided by UT-Battelle, LLC, under Contract No. DE-AC05-00OR22725 with the DOE, and sponsored by the Laboratory Directed Research and Development Program of Oak Ridge National Laboratory, managed by UT-Battelle, LLC, for the U.S. Department of Energy.

■ REFERENCES

(1) Naik, G. V.; Shalaev, V. M.; Boltasseva, A. Alternative plasmonic materials: beyond gold and silver. *Adv. Mater.* **2013**, *25*, 3264−3294.

(2) Agrawal, A.; Cho, S. H.; Zandi, O.; Ghosh, S.; Johns, R. W.; Milliron, D. J. Localized surface plasmon resonance in semiconductor nanocrystals. *Chem. Rev.* **2018**, *118*, 3121−3207.

(3) Agrawal, A.; Johns, R. W.; Milliron, D. J. Control of localized surface plasmon resonances in metal oxide nanocrystals. *Annu. Rev. Mater. Res.* **2017**, *47*, 1−31.

(4) Mattox, T. M.; Ye, X.; Manthiram, K.; Schuck, P. J.; Alivisatos, A. P.; Urban, J. J. Chemical control of plasmons in metal chalcogenide and metal oxide nanostructures. *Adv. Mater.* **2015**, *27*, 5830−5837.

(5) Comin, A.; Manna, L. New materials for tunable plasmonic colloidal nanocrystals. *Chem. Soc. Rev.* **2014**, *43*, 3957−3975.

(6) Liu, Z.; Zhong, Y.; Shafei, I.; Borman, R.; Jeong, S.; Chen, J.; Losovyj, Y.; Gao, X.; Li, N.; Du, Y.; Sarnello, E.; Li, T.; Su, D.; Ma, W.; Ye, X. Tuning infrared plasmon resonances in doped metal-oxide nanocrystals through cation-exchange reactions. *Nat. Commun.* **2019**, *10*, 1−11.

(7) Dunkelberger, A. D.; Ellis, C. T.; Ratchford, D. C.; Giles, A. J.; Kim, M.; Kim, C. S.; Spann, B. T.; Vurgaftman, I.; Tischler, J. G.; Long, J. P.; Glembocki, O. J.; Owrutsky, J. C.; Caldwell, J. D. Active tuning of surface phonon polariton resonances via carrier photoinjection. *Nat. Photonics* **2018**, *12*, 50−56.

(8) Luther, J. M.; Jain, P. K.; Ewers, T.; Alivisatos, A. P. Localized surface plasmon resonances arising from free carriers in doped quantum dots. *Nat. Mater.* **2011**, *10*, 361−366.

(9) Jung, J.; Pedersen, T. G. Analysis of plasmonic properties of heavily doped semiconductors using full band structure calculations. *J. Appl. Phys.* **2013**, *113*, 114904.

(10) Zhao, Y.; Pan, H.; Lou, Y.; Qiu, X.; Zhu, J.; Burda, C. Plasmonic $Cu_{2-x}S$ nanocrystals: optical and structural properties of copper-deficient copper (I) sulfides. *J. Am. Chem. Soc.* **2009**, *131*, 4253−4261.

(11) Riha, S. C.; Johnson, D. C.; Prieto, A. L. Cu_2Se nanoparticles with tunable electronic properties due to a controlled solid-state phase transition driven by copper oxidation and cationic conduction. *J. Am. Chem. Soc.* **2011**, *133*, 1383−1390.

(12) Buonsanti, R.; Llordes, A.; Aloni, S.; Helms, B. A.; Milliron, D. J. Tunable infrared absorption and visible transparency of colloidal aluminum-doped zinc oxide nanocrystals. *Nano Lett.* **2011**, *11*, 4706−4710.

(13) Ginn, J. C.; Jarecki, R. L., Jr; Shaner, E. A.; Davids, P. S. Infrared plasmons on heavily-doped silicon. *J. Appl. Phys.* **2011**, *110*, 043110.

(14) Schimpf, A. M.; Thakkar, N.; Gunthardt, C. E.; Masiello, D. J.; Gamelin, D. R. Charge-tunable quantum plasmons in colloidal semiconductor nanocrystals. *ACS Nano* **2014**, *8*, 1065−1072.

(15) Smith, K. C.; Olafsson, A.; Hu, X.; Quillin, S. C.; Idrobo, J. C.; Collette, R.; Rack, P. D.; Camden, J. P.; Masiello, D. J. Direct Observation of Infrared Plasmonic Fano Antiresonances by a Nanoscale Electron Probe. *Phys. Rev. Lett.* **2019**, *123*, 177401.

(16) Aleshire, K.; Pavlovetc, I. M.; Collette, R.; Kong, X.-T.; Rack, P. D.; Zhang, S.; Masiello, D. J.; Camden, J. P.; Hartland, G. V.; Kuno, M. Far-field midinfrared superresolution imaging and spectroscopy of single high aspect ratio gold nanowires. *Proc. Natl. Acad. Sci. U. S. A.* **2020**, *117*, 2288−2293.

(17) Jones, A. C.; Olmon, R. L.; Skrabalak, S. E.; Wiley, B. J.; Xia, Y. N.; Raschke, M. B. Mid-IR plasmonics: near-field imaging of coherent plasmon modes of silver nanowires. *Nano Lett.* **2009**, *9*, 2553−2558.
(18) Stanley, R. Plasmonics in the mid-infrared. *Nat. Photonics* **2012**, *6*, 409−411.
(19) Wu, Y.; Hu, Z.; Kong, X.-T.; Idrobo, J. C.; Nixon, A. G.; Rack, P. D.; Masiello, D. J.; Camden, J. P. Infrared plasmonics: STEM-EELS characterization of Fabry-Pérot resonance damping in gold nanowires. *Phys. Rev. B: Condens. Matter Mater. Phys.* **2020**, *101*, 085409.
(20) Bohren, C. F.; Huffman, D. R. *Absorption and scattering of light by small particles*; John Wiley & Sons: 2008.
(21) Hsu, S.-W.; Bryks, W.; Tao, A. R. Effects of Carrier Density and Shape on the Localized Surface Plasmon Resonances of Cu_2−xS Nanodisks. *Chem. Mater.* **2012**, *24*, 3765−3771.
(22) Kim, J.; Agrawal, A.; Krieg, F.; Bergerud, A.; Milliron, D. J. The interplay of shape and crystalline anisotropies in plasmonic semiconductor nanocrystals. *Nano Lett.* **2016**, *16*, 3879−3884.
(23) Abb, M.; Wang, Y.; Papasimakis, N.; De Groot, C.; Muskens, O. L. Surface-enhanced infrared spectroscopy using metal oxide plasmonic antenna arrays. *Nano Lett.* **2014**, *14*, 346−352.
(24) Yang, X.; Sun, Z.; Low, T.; Hu, H.; Guo, X.; García de Abajo, F. J.; Avouris, P.; Dai, Q. Nanomaterial-Based Plasmon-Enhanced Infrared Spectroscopy. *Adv. Mater.* **2018**, *30*, 1704896.
(25) Goel, S.; Chen, F.; Cai, W. Synthesis and biomedical applications of copper sulfide nanoparticles: from sensors to theranostics. *Small* **2014**, *10*, 631−645.
(26) Guo, M.; Law, W.-C.; Liu, X.; Cai, H.; Liu, L.; Swihart, M. T.; Zhang, X.; Prasad, P. N. Plasmonic semiconductor nanocrystals as chemical sensors: Pb^{2+} quantitation via aggregation-induced plasmon resonance shift. *Plasmonics* **2014**, *9*, 893−898.
(27) Baldassarre, L.; Sakat, E.; Frigerio, J.; Samarelli, A.; Gallacher, K.; Calandrini, E.; Isella, G.; Paul, D. J.; Ortolani, M.; Biagioni, P. Midinfrared plasmon-enhanced spectroscopy with germanium antennas on silicon substrates. *Nano Lett.* **2015**, *15*, 7225−7231.
(28) Hessel, C. M.; Pattani, V. P.; Rasch, M.; Panthani, M. G.; Koo, B.; Tunnell, J. W.; Korgel, B. A. Copper selenide nanocrystals for photothermal therapy. *Nano Lett.* **2011**, *11*, 2560−2566.
(29) Zhou, M.; Tian, M.; Li, C. Copper-based nanomaterials for cancer imaging and therapy. *Bioconjugate Chem.* **2016**, *27*, 1188−1199.
(30) Wu, Y.; Wadia, C.; Ma, W.; Sadtler, B.; Alivisatos, A. P. Synthesis and photovoltaic application of copper (I) sulfide nanocrystals. *Nano Lett.* **2008**, *8*, 2551−2555.
(31) Liu, L.; Zhou, B.; Deng, L.; Fu, W.; Zhang, J.; Wu, M.; Zhang, W.; Zou, B.; Zhong, H. Thermal annealing effects of plasmonic $Cu_{1.8}S$ nanocrystal films and their photovoltaic properties. *J. Phys. Chem. C* **2014**, *118*, 26964−26972.
(32) An, L.; Huang, L.; Liu, H.; Xi, P.; Chen, F.; Du, Y. High-Quality Copper Sulfide Nanocrystals with Diverse Shapes and Their Catalysis for Electrochemical Reduction of H_2O_2. *Particle & Particle Systems Characterization* **2015**, *32*, 536−541.
(33) Cui, G.; Wang, W.; Ma, M.; Xie, J.; Shi, X.; Deng, N.; Xin, J.; Tang, B. IR-Driven Photocatalytic Water Splitting with WO_2_Na_xWO_3 Hybrid Conductor Material. *Nano Lett.* **2015**, *15*, 7199−7203.
(34) Jiang, K.-Y.; Dai, X.-C.; Yu, Y.; Mo, Q.-L.; Xiao, F.-X. Boosting charge-transfer efficiency by simultaneously tuning double effects of metal nanocrystal in Z-scheme photocatalytic redox system. *J. Phys. Chem. C* **2018**, *122*, 12291−12306.
(35) Willets, K. A.; Van Duyne, R. P. Localized surface plasmon resonance spectroscopy and sensing. *Annu. Rev. Phys. Chem.* **2007**, *58*, 267−297.
(36) Taliercio, T.; Biagioni, P. Semiconductor infrared plasmonics. *Nanophotonics* **2019**, *8*, 949−990.
(37) Hu, M.; Novo, C.; Funston, A.; Wang, H.; Staleva, H.; Zou, S.; Mulvaney, P.; Xia, Y.; Hartland, G. V. Dark-field microscopy studies of single metal nanoparticles: understanding the factors that influence the linewidth of the localized surface plasmon resonance. *J. Mater. Chem.* **2008**, *18*, 1949−1960.
(38) Cao, W.; Huang, T.; Xu, X.-H. N.; Elsayed-Ali, H. E. Localized surface plasmon resonance of single silver nanoparticles studied by dark-field optical microscopy and spectroscopy. *J. Appl. Phys.* **2011**, *109*, 034310.
(39) Lindfors, K.; Kalkbrenner, T.; Stoller, P.; Sandoghdar, V. Detection and spectroscopy of gold nanoparticles using supercontinuum white light confocal microscopy. *Phys. Rev. Lett.* **2004**, *93*, 037401.
(40) Zayats, A. V.; Smolyaninov, I. I.; Maradudin, A. A. Nano-optics of surface plasmon polaritons. *Phys. Rep.* **2005**, *408*, 131−314.
(41) Keilmann, F.; Hillenbrand, R. Near-field microscopy by elastic light scattering from a tip. *Philos. Trans. R. Soc., A* **2004**, *362*, 787−805.
(42) Raschke, M. B.; Molina, L.; Elsaesser, T.; Kim, D. H.; Knoll, W.; Hinrichs, K. Apertureless Near-Field Vibrational Imaging of Block-Copolymer Nanostructures with Ultrahigh Spatial Resolution. *ChemPhysChem* **2005**, *6*, 2197−2203.
(43) Bechtel, H. A.; Muller, E. A.; Olmon, R. L.; Martin, M. C.; Raschke, M. B. Ultrabroadband infrared nanospectroscopic imaging. *Proc. Natl. Acad. Sci. U. S. A.* **2014**, *111*, 7191−7196.
(44) Khatib, O.; Bechtel, H. A.; Martin, M. C.; Raschke, M. B.; Carr, G. L. Far infrared synchrotron near-field nanoimaging and nanospectroscopy. *ACS Photonics* **2018**, *5*, 2773−2779.
(45) Johns, R. W.; Bechtel, H. A.; Runnerstrom, E. L.; Agrawal, A.; Lounis, S. D.; Milliron, D. J. Direct observation of narrow mid-infrared plasmon linewidths of single metal oxide nanocrystals. *Nat. Commun.* **2016**, *7*, 1−6.
(46) Krivanek, O. L.; Lovejoy, T. C.; Dellby, N.; Aoki, T.; Carpenter, R. W.; Rez, P.; Soignard, E.; Zhu, J.; Batson, P. E.; Lagos, M. J.; Egerton, R. F.; Crozier, P. A. Vibrational spectroscopy in the electron microscope. *Nature* **2014**, *514*, 209−212.
(47) Lovejoy, T.; Corbin, G.; Dellby, N.; Hoffman, M.; Krivanek, O. Advances in ultra-high energy resolution STEM-EELS. *Microsc. Microanal.* **2018**, *24*, 446−447.
(48) Hachtel, J. A.; Lupini, A. R.; Idrobo, J. C. Exploring the capabilities of monochromated electron energy loss spectroscopy in the infrared regime. *Sci. Rep.* **2018**, *8*, 1−10.
(49) Bel Hadj Tahar, R.; Ban, T.; Ohya, Y.; Takahashi, Y. Tin doped indium oxide thin films: Electrical properties. *J. Appl. Phys.* **1998**, *83*, 2631−2645.
(50) Minami, T. Transparent conducting oxide semiconductors for transparent electrodes. *Semicond. Sci. Technol.* **2005**, *20*, S35.
(51) Buchanan, M.; Webb, J.; Williams, D. Preparation of conducting and transparent thin films of tin-doped indium oxide by magnetron sputtering. *Appl. Phys. Lett.* **1980**, *37*, 213−215.
(52) Kim, H.; Gilmore, a. C.; Pique, A.; Horwitz, J.; Mattoussi, H.; Murata, H.; Kafafi, Z.; Chrisey, D. Electrical, optical, and structural properties of indium−tin−oxide thin films for organic light-emitting devices. *J. Appl. Phys.* **1999**, *86*, 6451−6461.
(53) Tuna, O.; Selamet, Y.; Aygun, G.; Ozyuzer, L. High quality ITO thin films grown by dc and RF sputtering without oxygen. *J. Phys. D: Appl. Phys.* **2010**, *43*, 055402.
(54) Brewer, S. H.; Franzen, S. Optical properties of indium tin oxide and fluorine-doped tin oxide surfaces: correlation of reflectivity, skin depth, and plasmon frequency with conductivity. *J. Alloys Compd.* **2002**, *338*, 73−79.
(55) Kanehara, M.; Koike, H.; Yoshinaga, T.; Teranishi, T. Indium tin oxide nanoparticles with compositionally tunable surface plasmon resonance frequencies in the near-IR region. *J. Am. Chem. Soc.* **2009**, *131*, 17736−17737.
(56) Ma, K.; Zhou, N.; Yuan, M.; Li, D.; Yang, D. Tunable surface plasmon resonance frequencies of monodisperse indium tin oxide nanoparticles by controlling composition, size, and morphology. *Nanoscale Res. Lett.* **2014**, *9*, 547.
(57) Crockett, B. M.; Jansons, A. W.; Koskela, K. M.; Johnson, D. W.; Hutchison, J. E. Radial dopant placement for tuning plasmonic properties in metal oxide nanocrystals. *ACS Nano* **2017**, *11*, 7719−7728.

https://dx.doi.org/10.1021/acs.nanolett.0c02772
Nano Lett. 2020, 20, 7987−7994

(58) Jansons, A. W.; Hutchison, J. E. Continuous growth of metal oxide nanocrystals: Enhanced control of nanocrystal size and radial dopant distribution. *ACS Nano* **2016**, *10*, 6942−6951.
(59) Zandi, O.; Agrawal, A.; Shearer, A. B.; Reimnitz, L. C.; Dahlman, C. J.; Staller, C. M.; Milliron, D. J. Impacts of surface depletion on the plasmonic properties of doped semiconductor nanocrystals. *Nat. Mater.* **2018**, *17*, 710−717.
(60) Gibbs, S. L.; Staller, C. M.; Milliron, D. J. Surface Depletion Layers in Plasmonic Metal Oxide Nanocrystals. *Acc. Chem. Res.* **2019**, *52*, 2516−2524.
(61) Cho, S. H.; Ghosh, S.; Berkson, Z. J.; Hachtel, J. A.; Shi, J.; Zhao, X.; Reimnitz, L. C.; Dahlman, C. J.; Ho, Y.; Yang, A.; Liu, Y.; Idrobo, J.-C.; Chmelka, B. F.; Milliron, D. J. Syntheses of Colloidal F:In_2O_3 cubes: Fluorine-Induced Faceting and Infrared Plasmonic Response. *Chem. Mater.* **2019**, *31*, 2661−2676.
(62) Cho, S. H.; Roccapriore, K. M.; Dass, C. K.; Ghosh, S.; Choi, J.; Noh, J.; Reimnitz, L. C.; Heo, S.; Kim, K.; Xie, K.; Korgel, B. A.; Li, X.; Hendrickson, J. R.; Hachtel, J. A.; Milliron, D. J. Spectrally tunable infrared plasmonic F,Sn:In_3O_3 nanocrystal cubes. *J. Chem. Phys.* **2020**, *152*, 014709.
(63) Kelly, K. L.; Coronado, E.; Zhao, L. L.; Schatz, G. C. The optical properties of metal nanoparticles: the influence of size, shape, and dielectric environment. *J. Phys. Chem. B* **2003**, *107*, 668−677.
(64) Tiggesbäumker, J.; Köller, L.; Meiwes-Broer, K.-H.; Liebsch, A. Blue shift of the Mie plasma frequency in Ag clusters and particles. *Phys. Rev. A: At., Mol., Opt. Phys.* **1993**, *48*, R1749.
(65) Scholl, J. A.; Koh, A. L.; Dionne, J. A. Quantum plasmon resonances of individual metallic nanoparticles. *Nature* **2012**, *483*, 421−427.
(66) Thakkar, N.; Montoni, N. P.; Cherqui, C.; Masiello, D. J. Plasmonic Landau damping in active environments. *Phys. Rev. B: Condens. Matter Mater. Phys.* **2018**, *97*, No. 121403(R).
(67) Monreal, R. C.; Antosiewicz, T. J.; Apell, S. P. Diffuse Surface Scattering and Quantum Size Effects in the Surface Plasmon Resonances of Low-Carrier-Density Nanocrystals. *J. Phys. Chem. C* **2016**, *120*, 5074−5082.
(68) Rosen, E. L.; Buonsanti, R.; Llordes, A.; Sawvel, A. M.; Milliron, D. J.; Helms, B. A. Exceptionally Mild Reactive Stripping of Native Ligands from Nanocrystal Surfaces by Using Meerwein's Salt. *Angew. Chem., Int. Ed.* **2012**, *51*, 684−689.
(69) Iberi, V.; Bigelow, N. W.; Mirsaleh-Kohan, N.; Griffin, S.; Simmons, P. D., Jr; Guiton, B. S.; Masiello, D. J.; Camden, J. P. Resonance-Rayleigh scattering and electron energy-loss spectroscopy of silver nanocubes. *J. Phys. Chem. C* **2014**, *118*, 10254−10262.
(70) Lagos, M. J.; Trügler, A.; Hohenester, U.; Batson, P. E. Mapping vibrational surface and bulk modes in a single nanocube. *Nature* **2017**, *543*, 529−532.
(71) Cherqui, C.; Li, G.; Busche, J. A.; Quillin, S. C.; Camden, J. P.; Masiello, D. J. Multipolar nanocube plasmon mode-mixing in finite substrates. *J. Phys. Chem. Lett.* **2018**, *9*, 504−512.
(72) Liu, W.; Cheng, S. Photoelectric properties of ITO thin films deposited by DC magnetron sputtering. *J. Semicond.* **2011**, *32*, 013002.
(73) Lounis, S. D.; Runnerstrom, E. L.; Bergerud, A.; Nordlund, D.; Milliron, D. J. Influence of Dopant Distribution on the Plasmonic Properties of Indium Tin Oxide Nanocrystals. *J. Am. Chem. Soc.* **2014**, *136*, 7110−7116.
(74) Tandon, B.; Agrawal, A.; Heo, S.; Milliron, D. J. Competition between depletion effects and coupling in the plasmon modulation of doped metal oxide nanocrystals. *Nano Lett.* **2019**, *19*, 2012−2019.
(75) Thoai, D. B. T.; Zeitler, E. Inelastic Scattering of Fast Electrons by Small Metal Particles. *Physica Status Solidi A* **1988**, *107*, 791−797.
(76) Echenique, P. M.; Bausells, J.; Rivacoba, A. Energy-loss probability in electron microscopy. *Phys. Rev. B: Condens. Matter Mater. Phys.* **1987**, *35*, 1521−1524.
(77) Pines, D.; Bohm, D. A Collective Description of Electron Interactions: II. Collective vs Individual Particle Aspects of the Interactions. *Phys. Rev.* **1952**, *85*, 338.
(78) Ritchie, R. H. Plasma Losses by Fast Electrons in Thin Films. *Phys. Rev.* **1957**, *106*, 874−881.
(79) García de Abajo, F. J. Optical excitations in electron microscopy. *Rev. Mod. Phys.* **2010**, *82*, 209.
(80) Egerton, R. F. *Electron energy-loss spectroscopy in the electron microscope*; Springer Science & Business Media: 2011.
(81) Wu, Y.; Li, G.; Camden, J. P. Probing nanoparticle plasmons with electron energy loss spectroscopy. *Chem. Rev.* **2018**, *118*, 2994−3031.
(82) Reed, B.; Sarikaya, M. Background subtraction for low-loss transmission electron energy-loss spectroscopy. *Ultramicroscopy* **2002**, *93*, 25−37.
(83) Egerton, R. F. Electron energy-loss spectroscopy in the TEM. *Rep. Prog. Phys.* **2009**, *72*, 016502.
(84) Kischkat, J.; Peters, S.; Gruska, B.; Semtsiv, M.; Chashnikova, M.; Klinkmüller, M.; Fedosenko, O.; Machulik, S.; Aleksandrova, A.; Monastyrskyi, G.; Flores, Y.; Masselink, W. T. Mid-infrared optical properties of thin films of aluminum oxide, titanium oxide, silicon dioxide, aluminum nitride, and silicon nitride. *Appl. Opt.* **2012**, *51*, 6789−6798.
(85) Cai, S.; Lu, B.; Chen, H.; Pan, J.; Chen, P. Homogeneous $(Lu_{1-x}In_x)_2O_3 (x = 0 - 1)$ solid solutions: Controlled synthesis, structure features and optical properties. *Powder Technol.* **2017**, *317*, 224−229.
(86) Liu, Q.; Quillin, S. C.; Masiello, D. J.; Crozier, P. A. Nanoscale probing of resonant photonic modes in dielectric nanoparticles with focused electron beams. *Phys. Rev. B: Condens. Matter Mater. Phys.* **2019**, *99*, 165102.
(87) Hamberg, I.; Granqvist, C. G. Evaporated Sn-doped In_2O_3 films: Basic optical properties and applications to energy-efficient windows. *J. Appl. Phys.* **1986**, *60*, 123−159.
(88) Weijtens, C. H. L.; van Loon, P. A. C. Influence of annealing on the optical properties of indium tin oxide. *Thin Solid Films* **1991**, *196*, 1−10.
(89) Gerfin, T.; Grätzel, M. Optical properties of tin-doped indium oxide determined by spectroscopic ellipsometry. *J. Appl. Phys.* **1996**, *79*, 1722−1729.
(90) Köstlin, H.; Jost, R.; Lems, W. Optical and electrical properties of doped In_2O_3 films. *Physica Status Solidi A* **1975**, *29*, 87−93.
(91) Ohhata, Y.; Shinoki, F.; Yoshida, S. Optical properties of r.f. reactive sputtered tin-doped In_2O_3 films. *Thin Solid Films* **1979**, *59*, 255−261.
(92) Szczyrbowski, J.; Schmalzbauer, K.; Hoffmann, H. Optical properties of In_2O_3−SnO_2 films in the transparent and plasma reflection region. *Thin Solid Films* **1986**, *137*, 169−183.
(93) Vial, A.; Grimault, A.-S.; Macías, D.; Barchiesi, D.; de la Chapelle, M. L. Improved analytical fit of gold dispersion: Application to the modeling of extinction spectra with a finite-difference time-domain method. *Phys. Rev. B: Condens. Matter Mater. Phys.* **2005**, *71*, 085416.
(94) Olmon, R. L.; Slovick, B.; Johnson, T. W.; Shelton, D.; Oh, S.-H.; Boreman, G. D.; Raschke, M. B. Optical dielectric function of gold. *Phys. Rev. B: Condens. Matter Mater. Phys.* **2012**, *86*, 235147.
(95) Kim, B. H.; Staller, C. M.; Cho, S. H.; Heo, S.; Garrison, C. E.; Kim, J.; Milliron, D. J. High mobility in nanocrystal-based transparent conducting oxide thin films. *ACS Nano* **2018**, *12*, 3200−3208.
(96) Steinhauser, J.; Fay, S.; Oliveira, N.; Vallat-Sauvain, E.; Ballif, C. Transition between grain boundary and intragrain scattering transport mechanisms in boron-doped zinc oxide thin films. *Appl. Phys. Lett.* **2007**, *90*, 142107.
(97) Guillén, C.; Herrero, J. Structural and plasmonic characteristics of sputtered SnO_2:Sb and ZnO:Al thin films as a function of their thickness. *J. Mater. Sci.* **2016**, *51*, 7276−7285.
(98) Cherqui, C.; Thakkar, N.; Li, G.; Camden, J. P.; Masiello, D. J. Characterizing Localized Surface Plasmons Using Electron Energy-Loss Spectroscopy. *Annu. Rev. Phys. Chem.* **2016**, *67*, 331−357.

https://dx.doi.org/10.1021/acs.nanolett.0c02772
Nano Lett. 2020, 20, 7987−7994